Contents

1 Introduction

The measurements were carried out on September 10, 2015, after the tuning process was finished.

2 Temperature drift of SENIS probe

The transducers from SENIS reading out the Hall probe voltages have shown to give a signal that varies with the temperature of the electronics in the transducers. The electronics is equipped with a temperature sensor and it is possible to follow the temperature variations of the elctronics in the thesducers. On September 8, 2015, a test was carried out where the undulator was at minimum fixed gap and the value for the vertical field and the temperature was recorded for approximateley 4 h. Figure 1 shows the measured temperature and vertical magnetic field during the test. As can be seenin Figure 1, the temperature of the transducer electronics and the output value for the vertical fiald are correlated.

Figure 2 shows the correleation of the output value for the vertical field and temeprature of the electronics during the test. The linear fit in Figure 2 can be used to create a temperature correction function:

$$B_{yCorr} = B_y \times (1 + 0.000808 \times (T_{SENIS} - 22)) \quad (1)$$

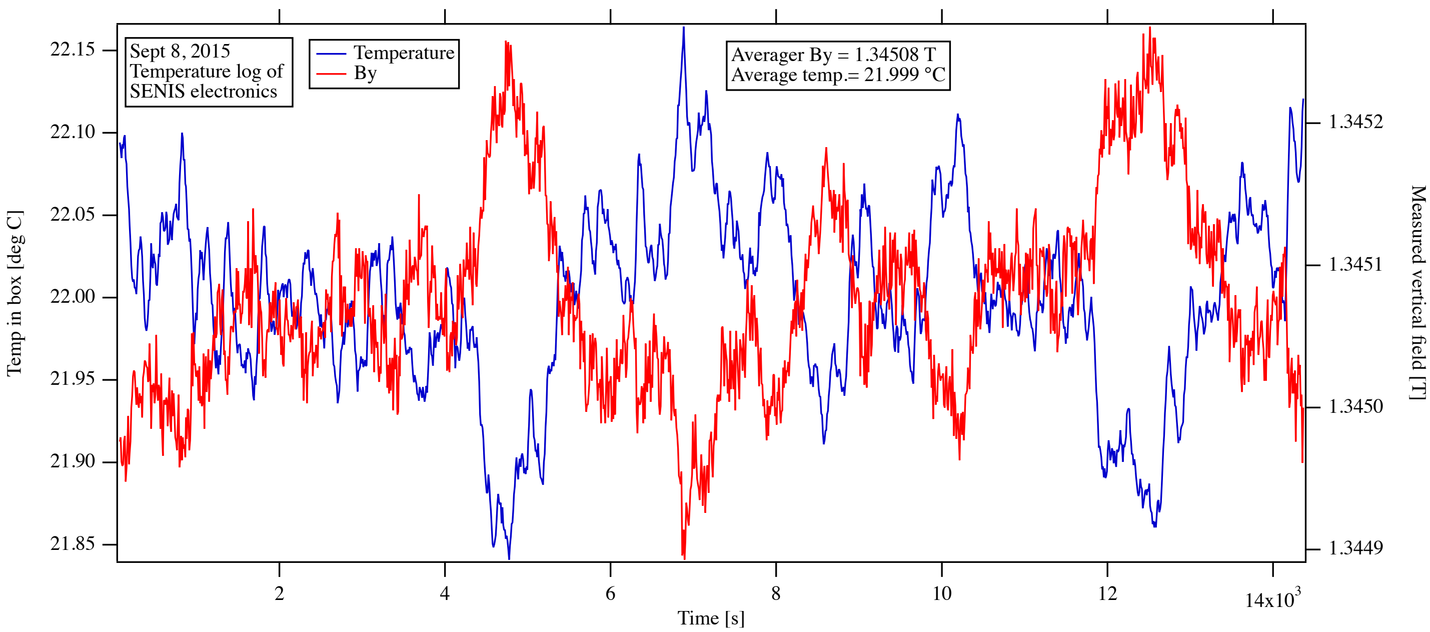

Figure 1: Measured temperature of the elctronics in the transducer and vertical magnetic field during an approximately 4 h long test run on Septeber 8, 2015.

where it has been assumed that the normal temperature of the SENIS elctronics is 22°. B_{yCorr} is the temperature corrected Hall probe reading. B_y is the Hall probe reading. T_{SENIS} is the temperature of the Hall probe electronics. Figure 3 shows the temperature corrected Hall probe reading compared to the orginal output values from the Hall probe measuring a vertical field.

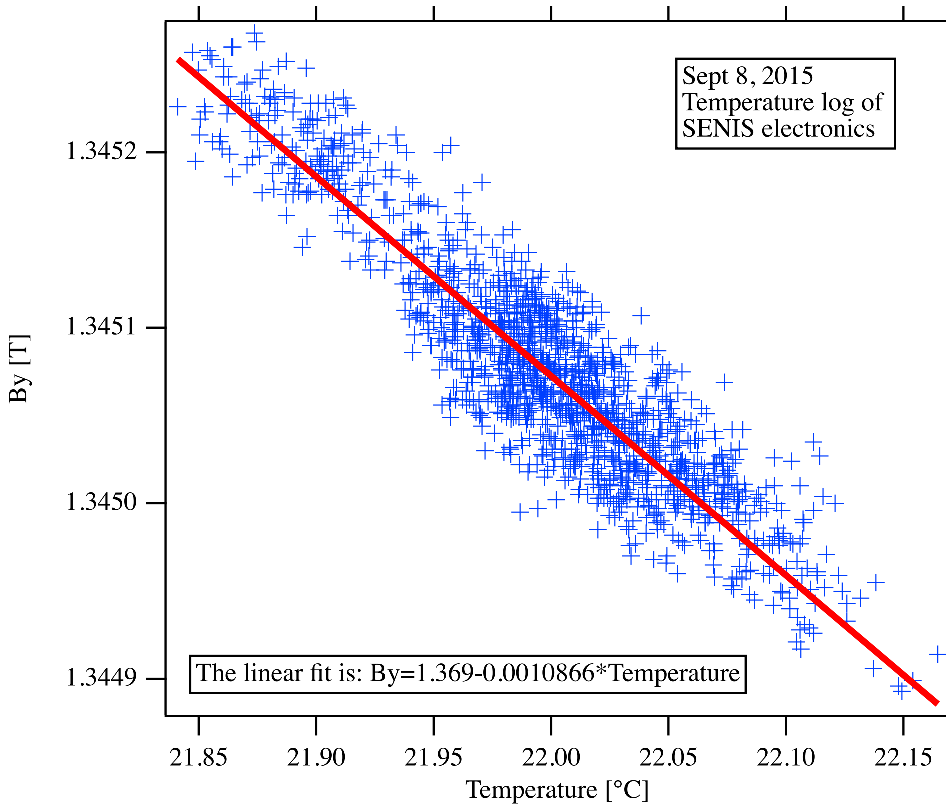

Figure 2: Correleation of the output value for the vertical field and temeprature of the electronics during the 4 h long test shown in Figure 1.

As from September 8, 2015, the temperature of the SENIS electronics is recorded for every reading of the Hall probes and the correction function in Equation (1) is used for all Hall probe data.

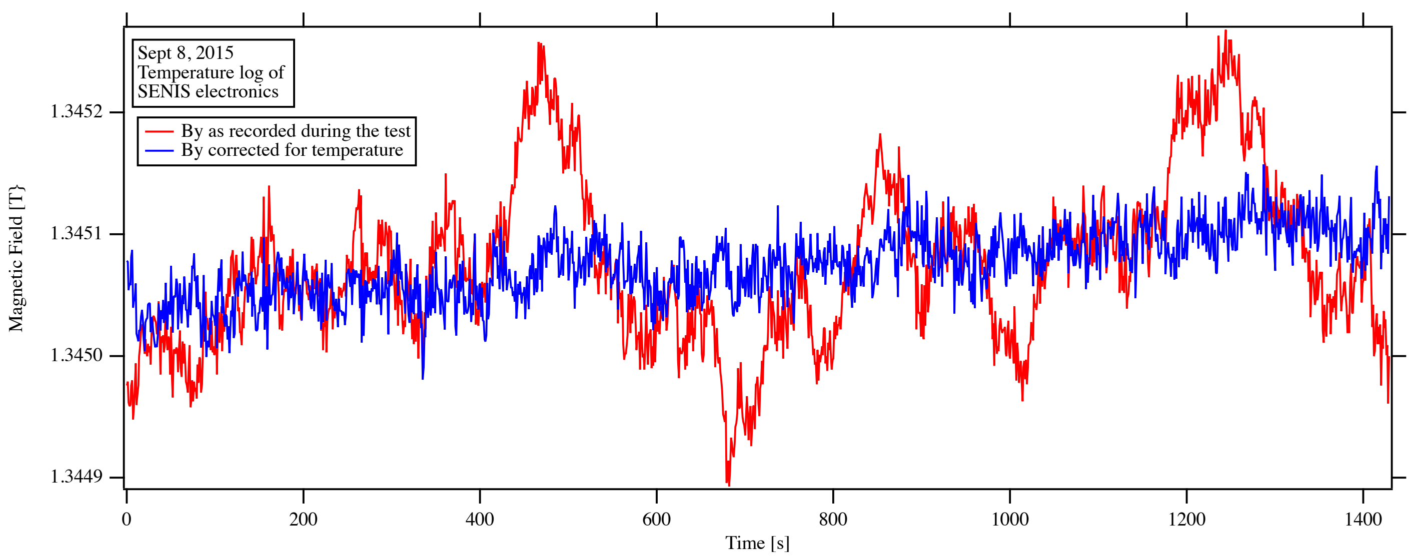

Figure 3: Measured and temperature corrected vertical magnetic field during the approximately 4 h long test run on Septeber 8, 2015.

3 Field integrals

The field integrals are measured with a 3.735 m long flip coil. The diameter of the flip coil is approximately 4 mm. The vertical and horizontal field integrals have been measured on the vertical axis out from the horizontal center of the undulator in 2 mm steps out to ±20 mm horizontal deviation from the undulator axis. The multipoles up to octupole order have been found by fitting a cubic polynomial over the five central points over ±4 mm horizontal deviation from the undulator axis.

3.1 Vertical field integrals

Figure 4 shows the measured vertical field integrals at 9 different gaps. Table 1 gives the multipoles calculated from the measured field integrals by using a cubic polynomila over the 5 central points over the horizontal range ±4 mm out from the undulator axis. The background vertical field integral in UMF measured without an undulator installed is -125 Gcm.

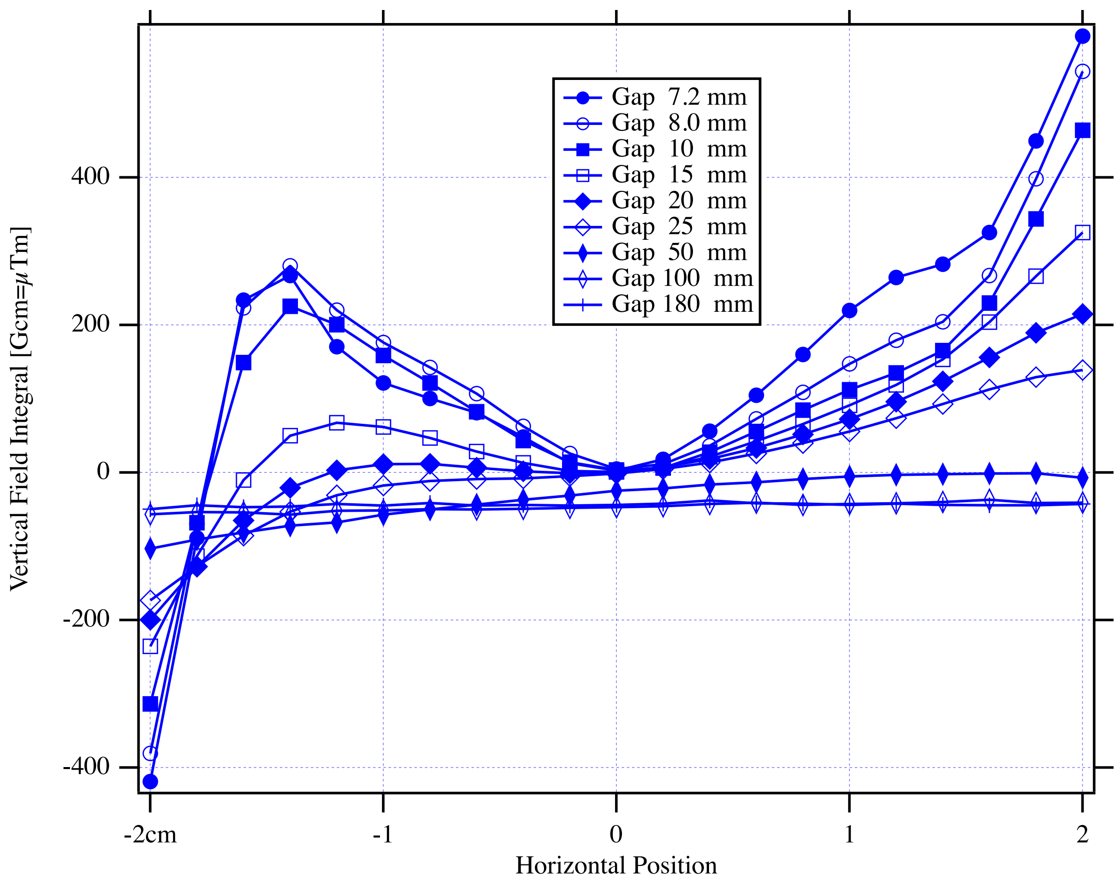

Figure 4: Vertical field integrals measured with a 3.735 m long flip coil.

3.2 Horizontal field integrals

Figure 5 shows the measured horizontal field integrals at 9 different gaps. Table 2 gives the skew multipoles calculated from the measured field integrals by using a cubic polynomila over the 5 central points over the horizontal range ±4 mm out from the undulator axis. The background horizontal field integral in UMF measured without an undulator installed is 47 Gcm.

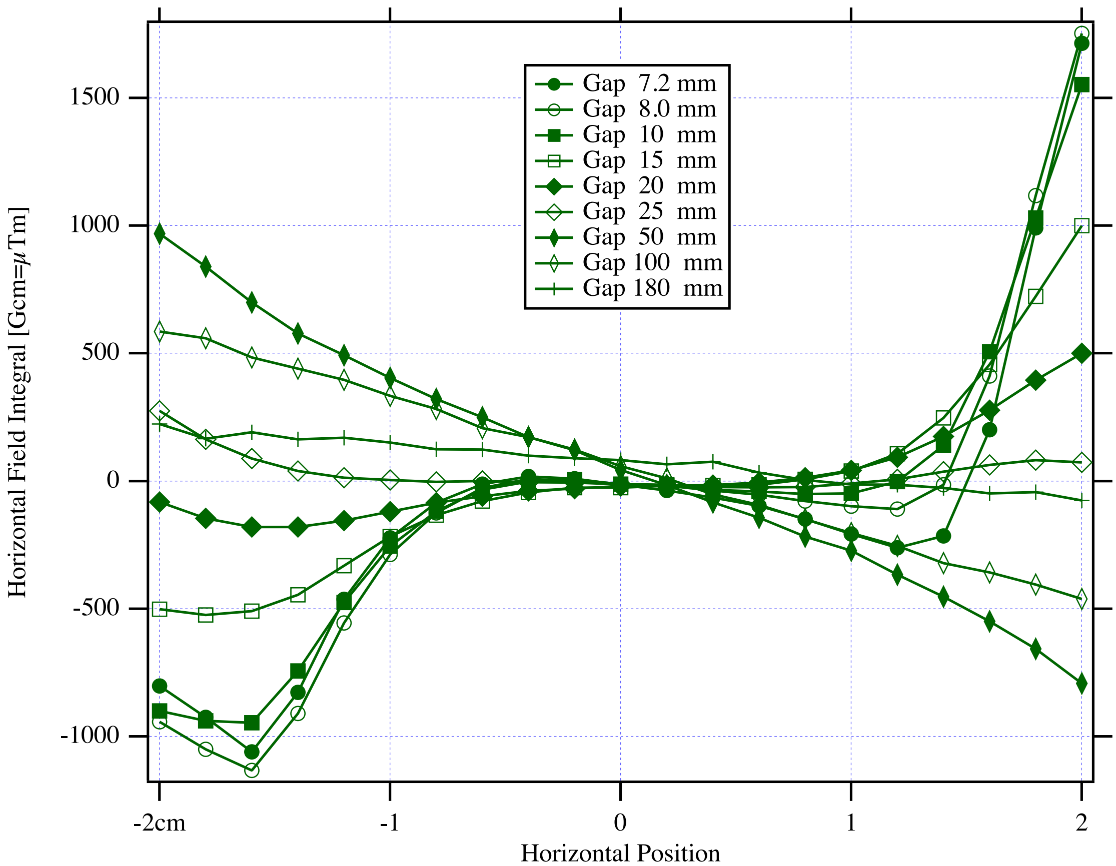

Figure 5: Horizontal field integrals measured with a 3.735 m long flip coil.

Table 1: Normal, i.e. vertical, multipoles.

Gap mm	Dipole Gcm	Quadrupole G	Sextupole G/cm	Octupole G/cm^2
7.2	3 ±0.3	14 ±1.9	310 ±2.6	-21 ±13
8	7 ±1.8	-38 ±12.5	271 ±17.6	31 ±86.8
10	3 ±1	-19 ±7.1	206 ±10	-3 ±49.5
15	1 ±0.2	12 ±1.3	102 ±1.8	-12 ±9
20	1 ±0.2	20 ±1.2	58 ±1.7	4 ±8.2
25	-1 ±0.1	22 ±0.5	24 ±0.7	32 ±3.2
50	-25 ±0.9	23 ±6	-9 ±8.5	14 ±41.9
100	-47 ±0	6 ±0.1	7 ±0.1	19 ±0.7
180	-44 ±0.2	6 ±1.2	19 ±1.7	6 ±8.4

Table 2: Skew, i.e. horizontal, multipoles.

Gap mm	Dipole Gcm	Quadrupole G	Sextupole G/cm	Octupole G/cm^2
7.2	-12 ±1.7	-120 ±11.7	-66 ±16.4	97 ±81.1
8	-11 ±4.9	-45 ±33.3	-18 ±46.8	-77 ±230.7
10	-5 ±6.4	-52 ±43.6	-72 ±61.4	62 ±302.6
15	-22 ±3.6	17 ±24.3	-50 ±34.1	107 ±168.3
20	-21 ±1.4	28 ±9.4	-39 ±13.2	9 ±64.9
25	-11 ±1.8	-28 ±12.6	-13 ±17.7	31 ±87.1
50	50 ±6.1	-347 ±41.4	-24 ±58.3	181 ±287.4
100	64 ±5.8	-285 ±39.7	-16 ±55.8	23 ±275
180	78 ±4	-68 ±27.1	59 ±38.1	242 ±187.8

4 Measured fields, angles, trajectories and phase errors

The magnetic fields have been measured on the undulator axis in 4400 mm long Hall probe scans. The field integral found with the flip coil is used for normalizing the magetic fields measured with the Hall probe system. The normalization is done by adding or subratcing a constant field over the magnetic structure of the undulator. The constant that is added corresponds to the difference between the flip coil and the Hall probe data over the length of the flip coil.

The Hall probe scans have been carried out at 9 different gaps; 7.2, 8.0, 10, 15, 20, 25, 50, 100, and 180 mm. The magnetic fields have been analyzed for the gap range 7.2-25 mm. In the analysis the function of the aoutocorrection system for the beam position in the accelerator has been simulated by using virtual coils in the beginning and end of the 4.4 m long scan to correct the orbit of the beam passing through the undulator.

4.1 Gap 7.2 mm

The measured fields, angles, trajectories and phase errors for the HXU-32 at 7.2 mm gap is shown in Figure 6 and Figure 7, which shows the same analysis with the beam path corrected by virtual coils in the beginning and end of the scan.

4.2 Gap 8.0 mm

The measured fields, angles, trajectories and phase errors for the HXU-32 at 8.0 mm gap is shown in Figure 8 and Figure 9, which shows the same analysis with the beam path corrected by virtual coils in the beginning and end of the scan.

4.3 Gap 10 mm

The measured fields, angles, trajectories and phase errors for the HXU-32 at 10 mm gap is shown in Figure 10 and Figure 11, which shows the same analysis with the beam path corrected by virtual coils in the beginning and end of the scan.

4.4 Gap 15 mm

The measured fields, angles, trajectories and phase errors for the HXU-32 at 15 mm gap is shown in Figure 12 and Figure 13, which shows the same analysis with the beam path corrected by virtual coils in the beginning and end of the scan.

4.5 Gap 20 mm

The measured fields, angles, trajectories and phase errors for the HXU-32 at 20 mm gap is shown in Figure 14 and Figure 15, which shows the same analysis with the beam path corrected by virtual coils in the beginning and end of the scan.

4.6 Gap 25 mm

The measured fields, angles, trajectories and phase errors for the HXU-32 at 25 mm gap is shown in Figure 16 and Figure 17, which shows the same analysis with the beam path corrected by virtual coils in the beginning and end of the scan.

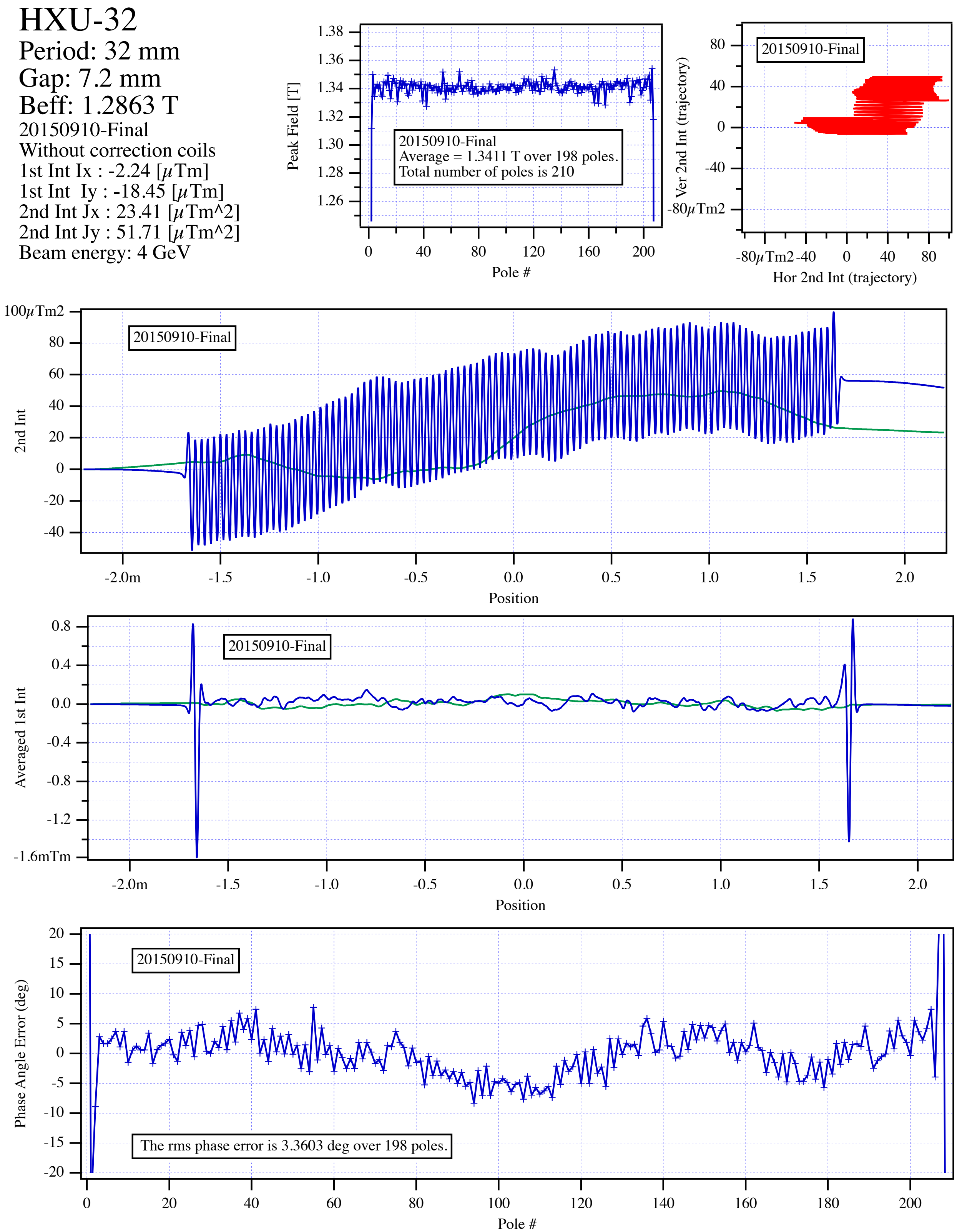

Figure 6: The measured fields, angles, trajectories and phase errors for the HXU-32 at 7.2 mm gap.

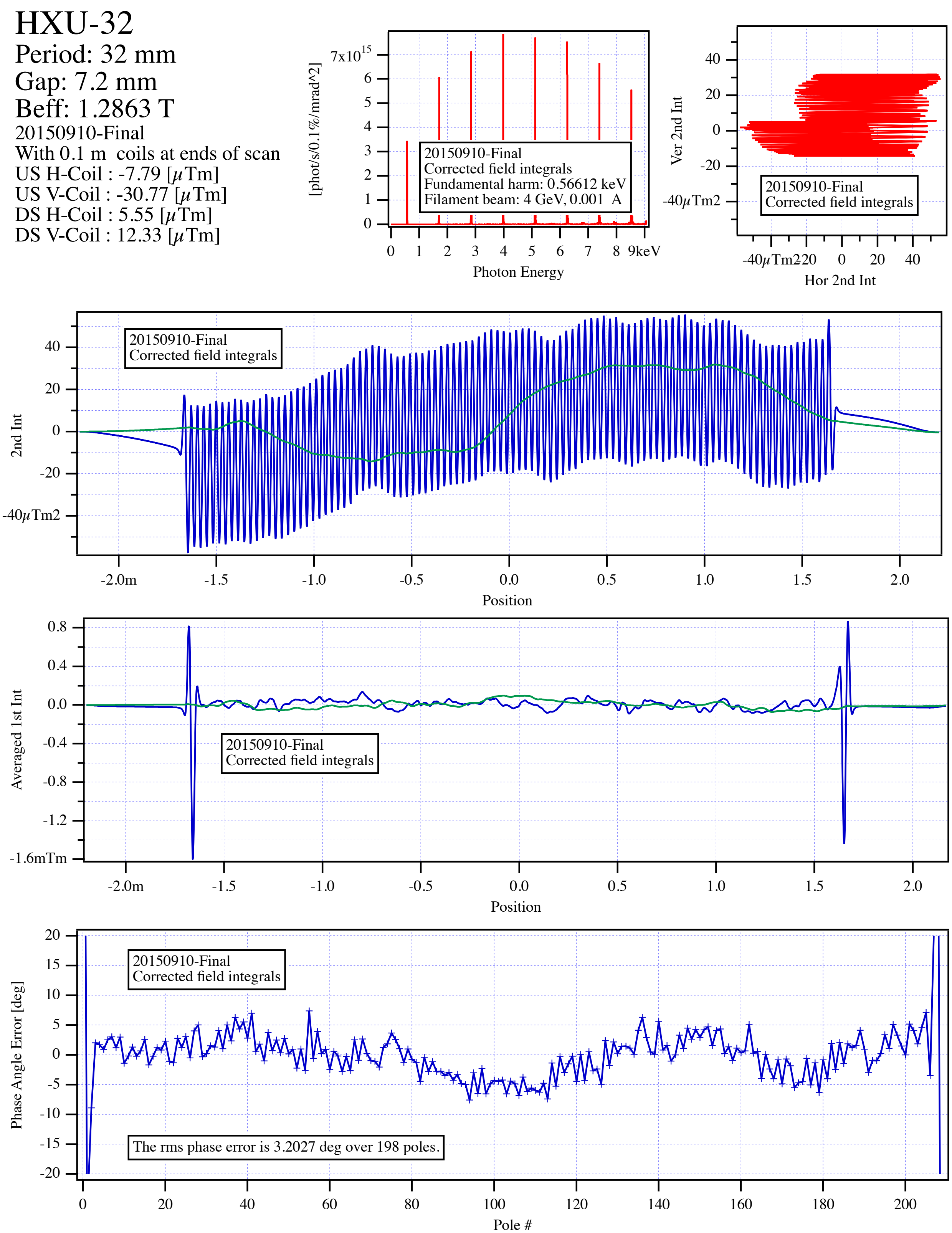

Figure 7: The measured fields, angles, trajectories and phase errors for the HXU-32 at 7.2 mm gap with the beam path corrected by virtual coils.

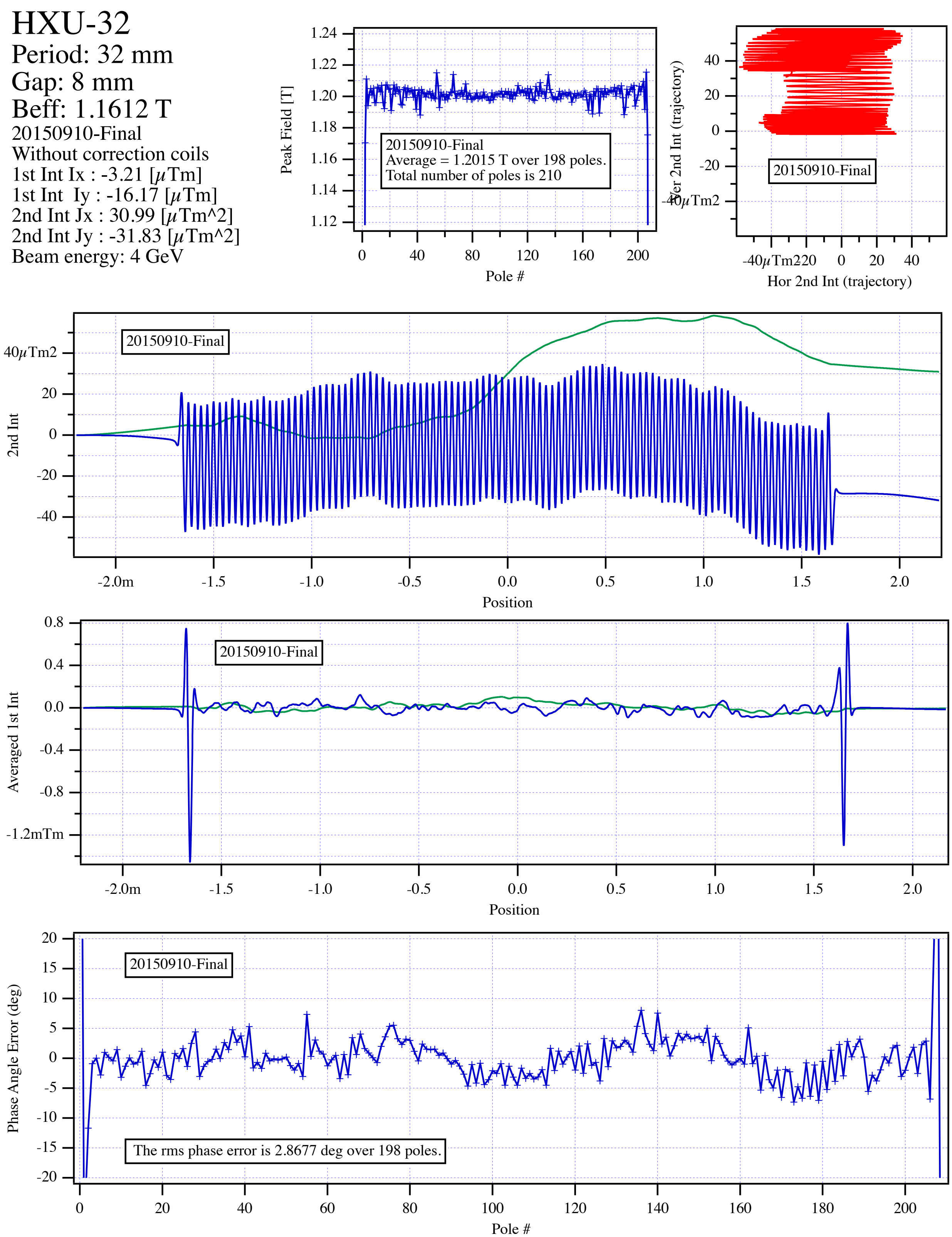

Figure 8: The measured fields, angles, trajectories and phase errors for the HXU-32 at 8.0 mm gap.

HXU-32
Period: 32 mm
Gap: 8 mm
Beff: 1.1615 T
20150910-Final
Without correction coils
1st Int Ix : -3.21 [μTm]
1st Int Iy : -16.22 [μTm]
2nd Int Jx : 31 [μTm^2]
2nd Int Jy : -31.74 [μTm^2]
Beam energy: 4 GeV

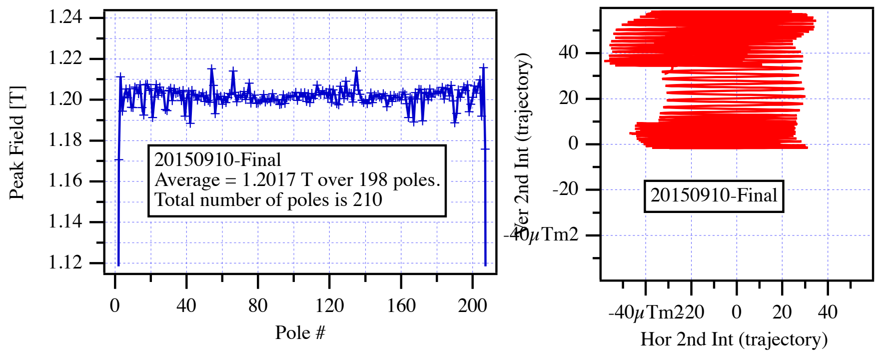

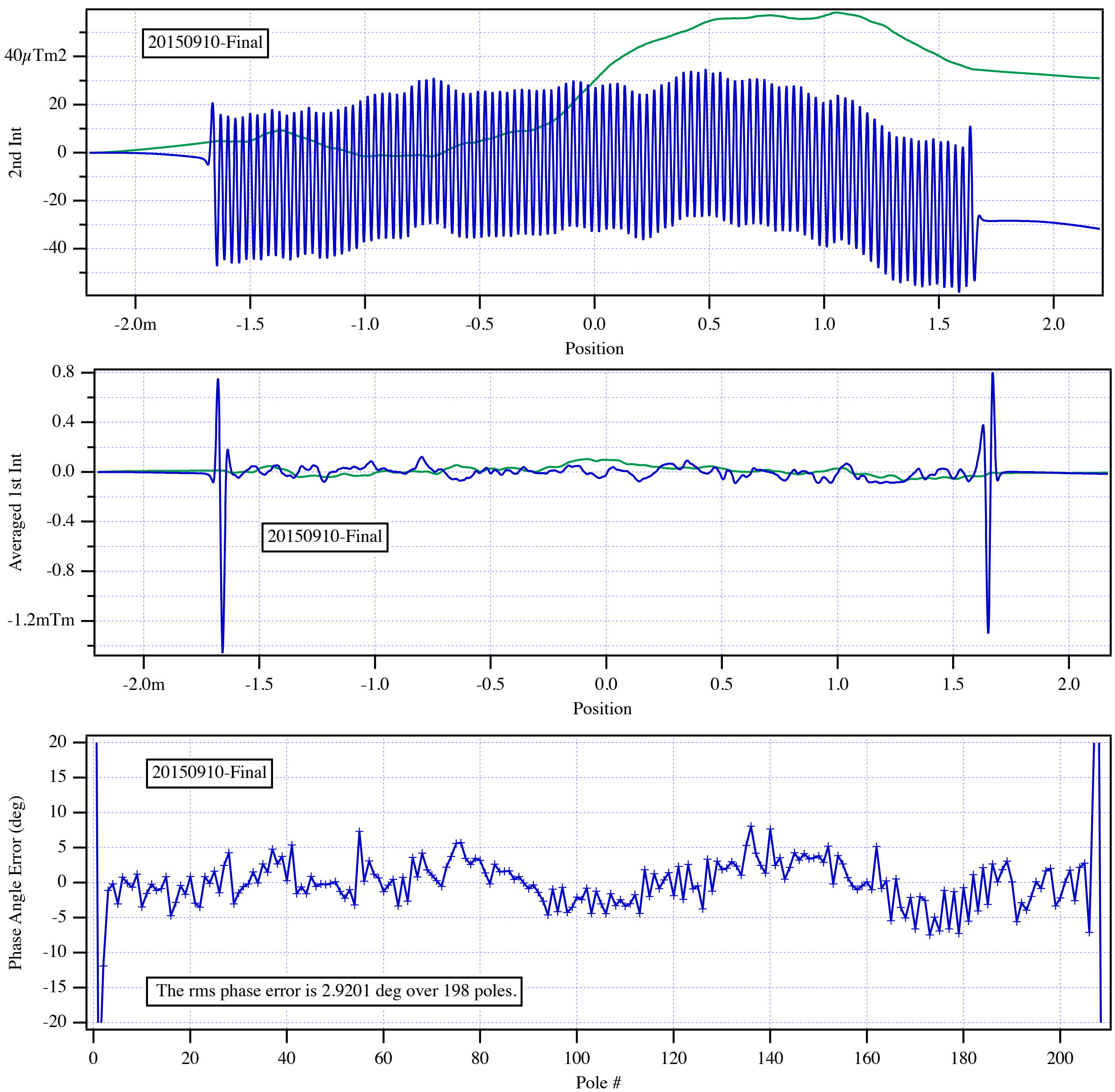

Figure 9: The measured fields, angles, trajectories and phase errors for the HXU-32 at 8.0 mm gap with the beam path corrected by virtual coils.

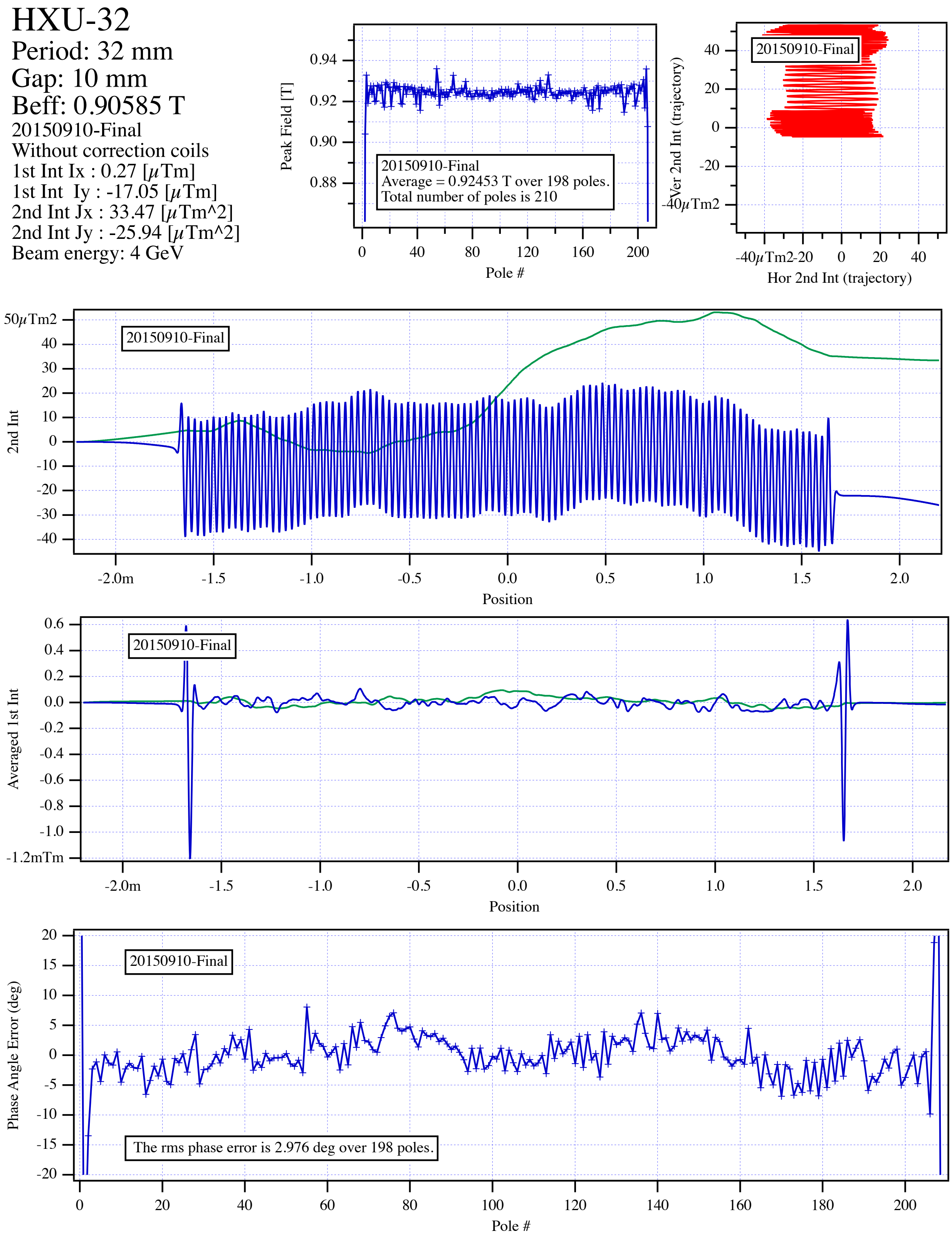

Figure 10: The measured fields, angles, trajectories and phase errors for the HXU-32 at 10 mm gap.

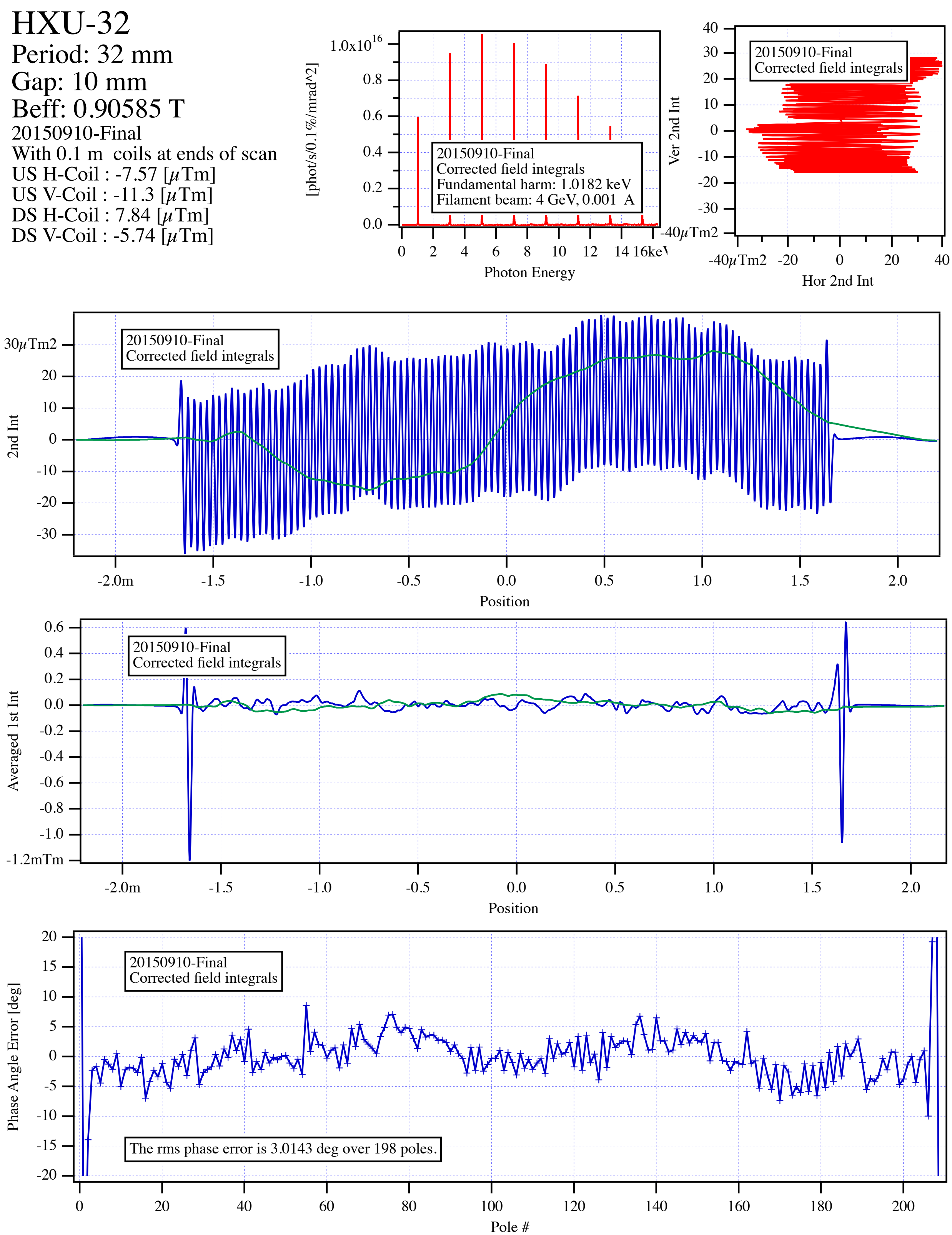

Figure 11: The measured fields, angles, trajectories and phase errors for the HXU-32 at 10 mm gap with the beam path corrected by virtual coils.

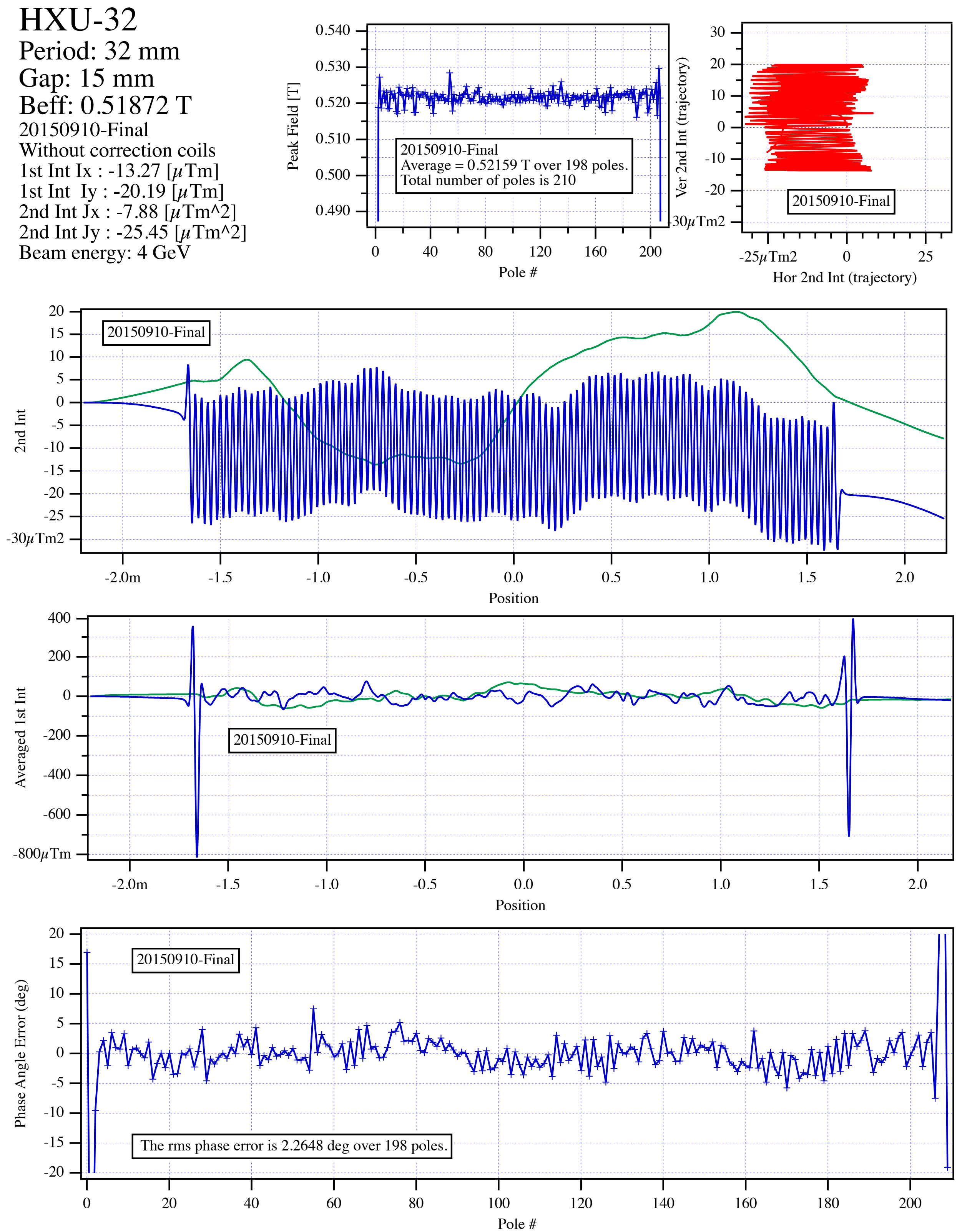

Figure 12: The measured fields, angles, trajectories and phase errors for the HXU-32 at 15 mm gap.

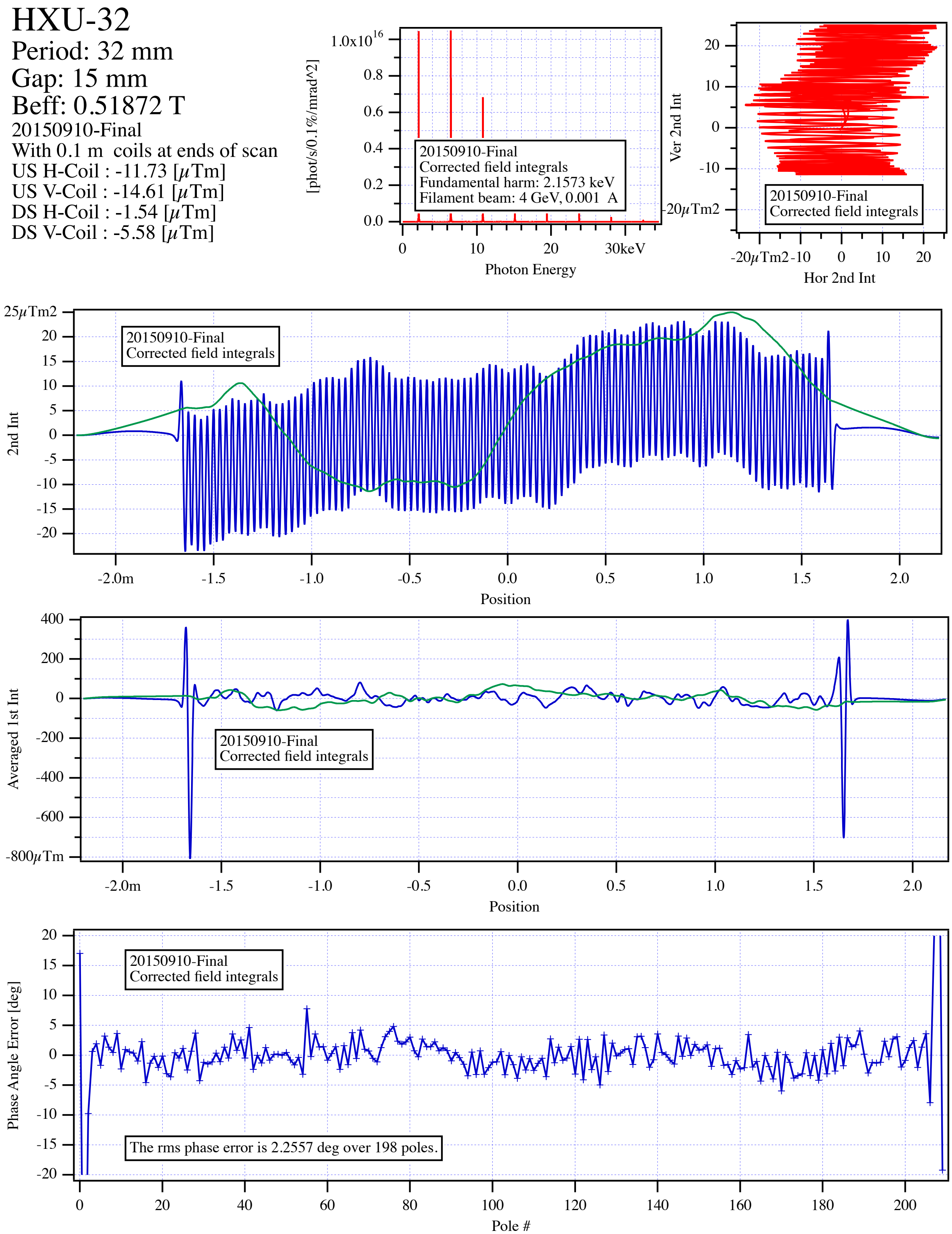

Figure 13: The measured fields, angles, trajectories and phase errors for the HXU-32 at 15 mm gap with the beam path corrected by virtual coils.

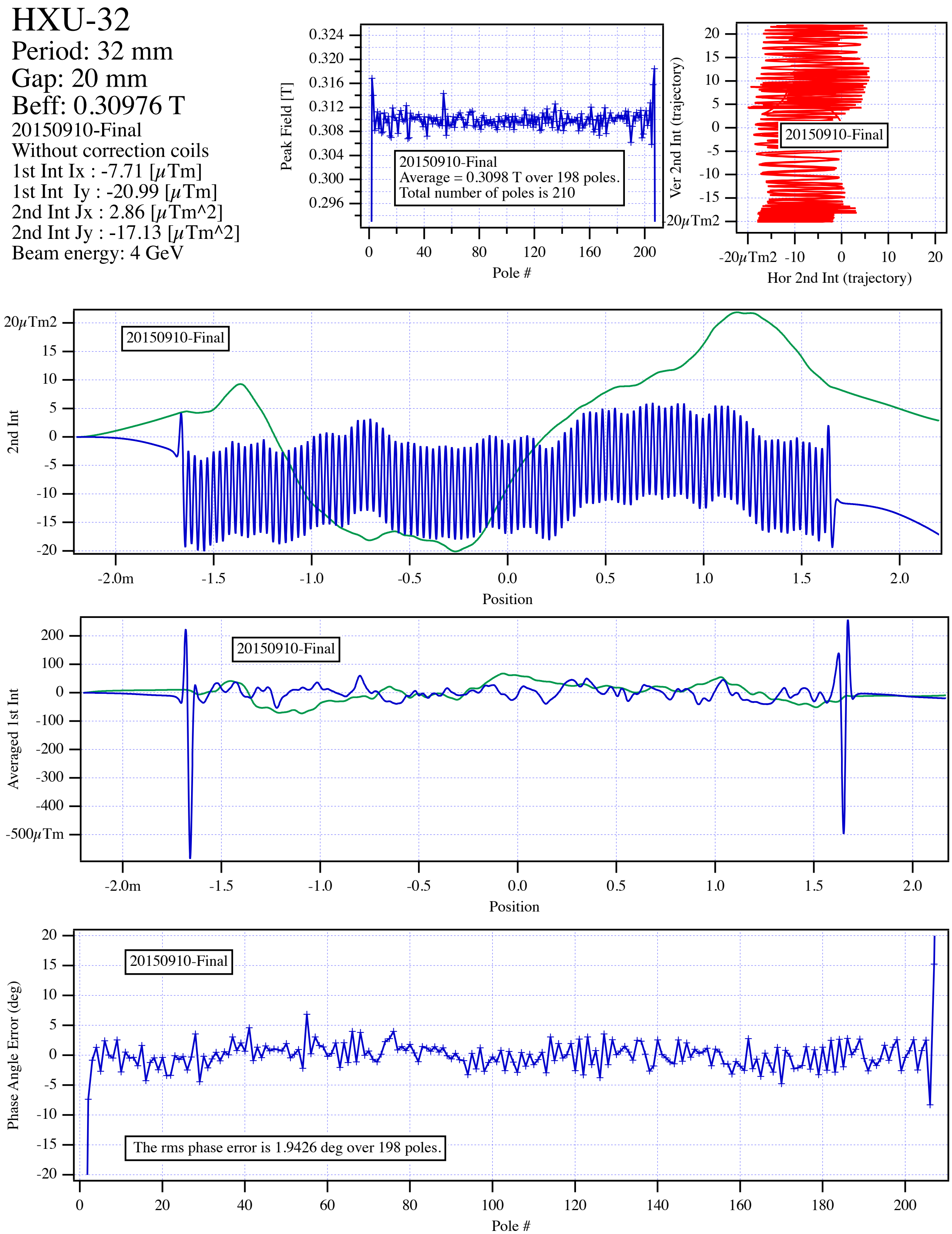

Figure 14: The measured fields, angles, trajectories and phase errors for the HXU-32 at 20 mm gap.

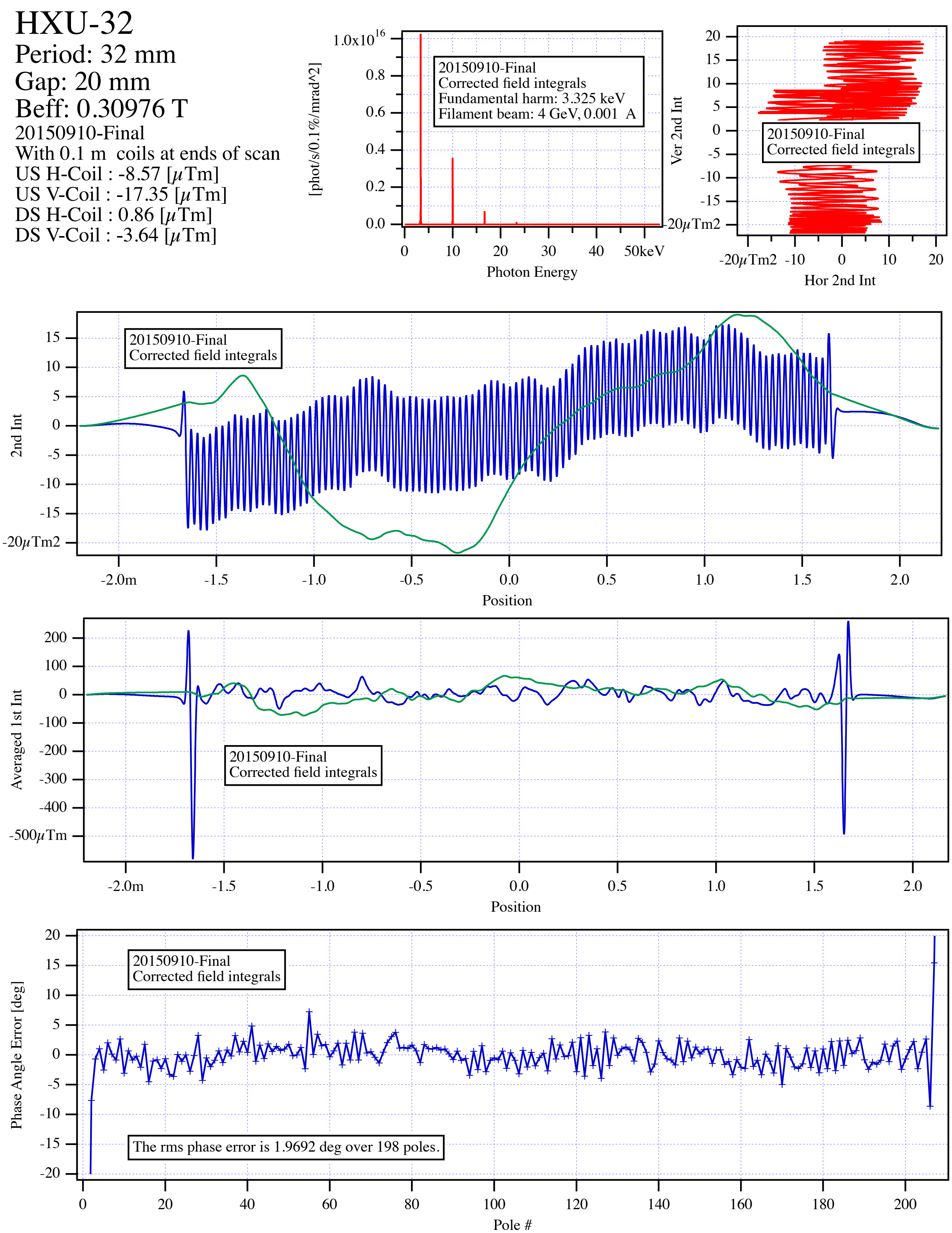

Figure 15: The measured fields, angles, trajectories and phase errors for the HXU-32 at 20 mm gap with the beam path corrected by virtual coils.

HXU-32
Period: 32 mm
Gap: 25 mm
Beff: 0.18759 T
20150910-Final
Without correction coils
1st Int Ix : -2.23 [μTm]
1st Int Iy : -22.65 [μTm]
2nd Int Jx : 17.86 [μTm^2]
2nd Int Jy : -13.3 [μTm^2]
Beam energy: 4 GeV

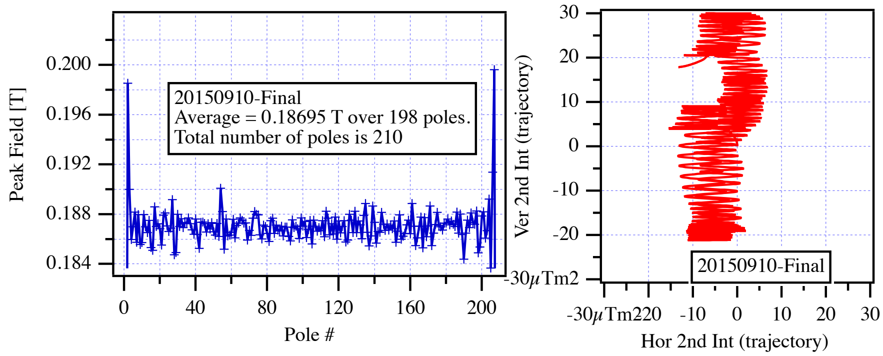

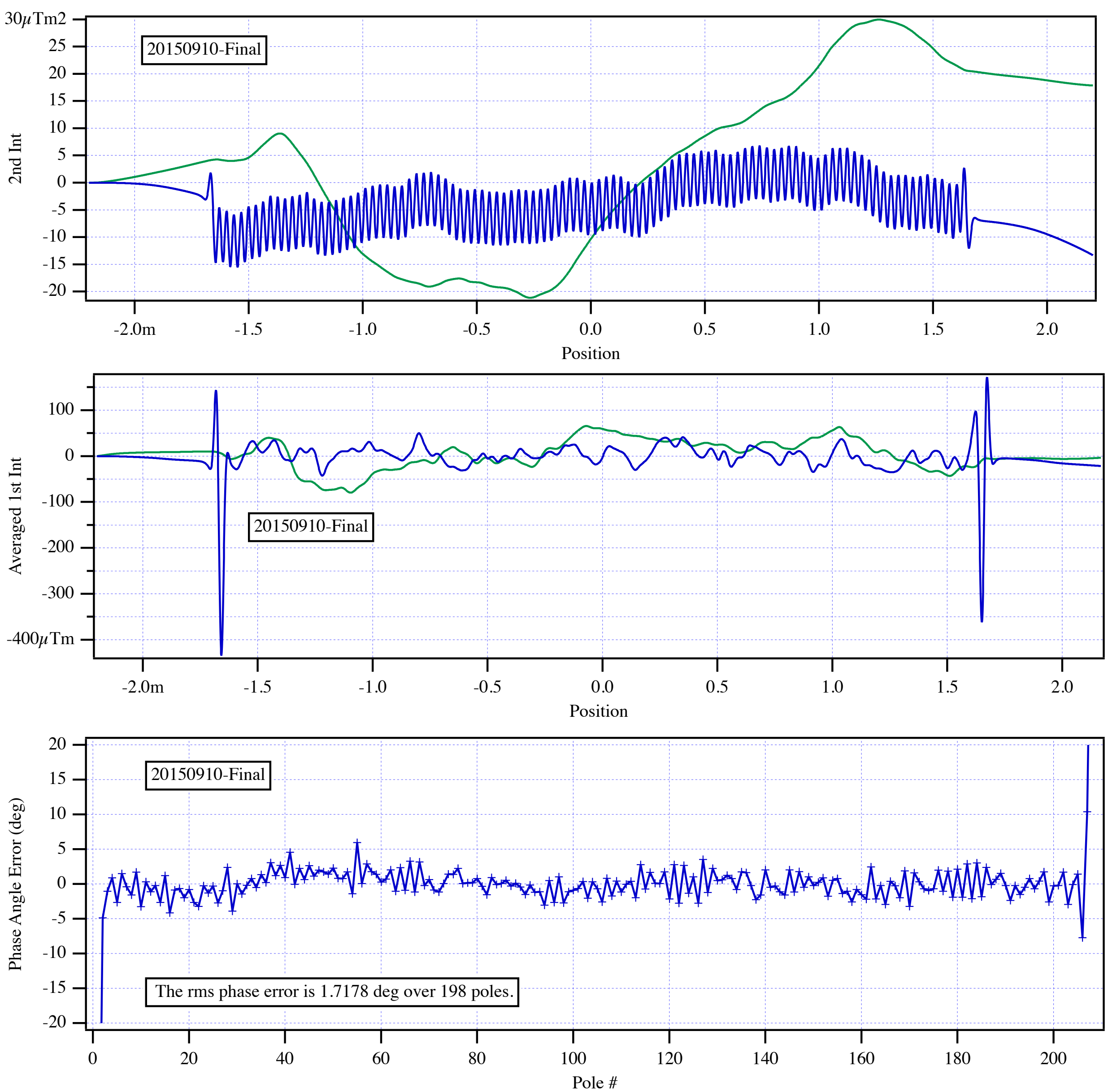

Figure 16: The measured fields, angles, trajectories and phase errors for the HXU-32 at 25 mm gap.

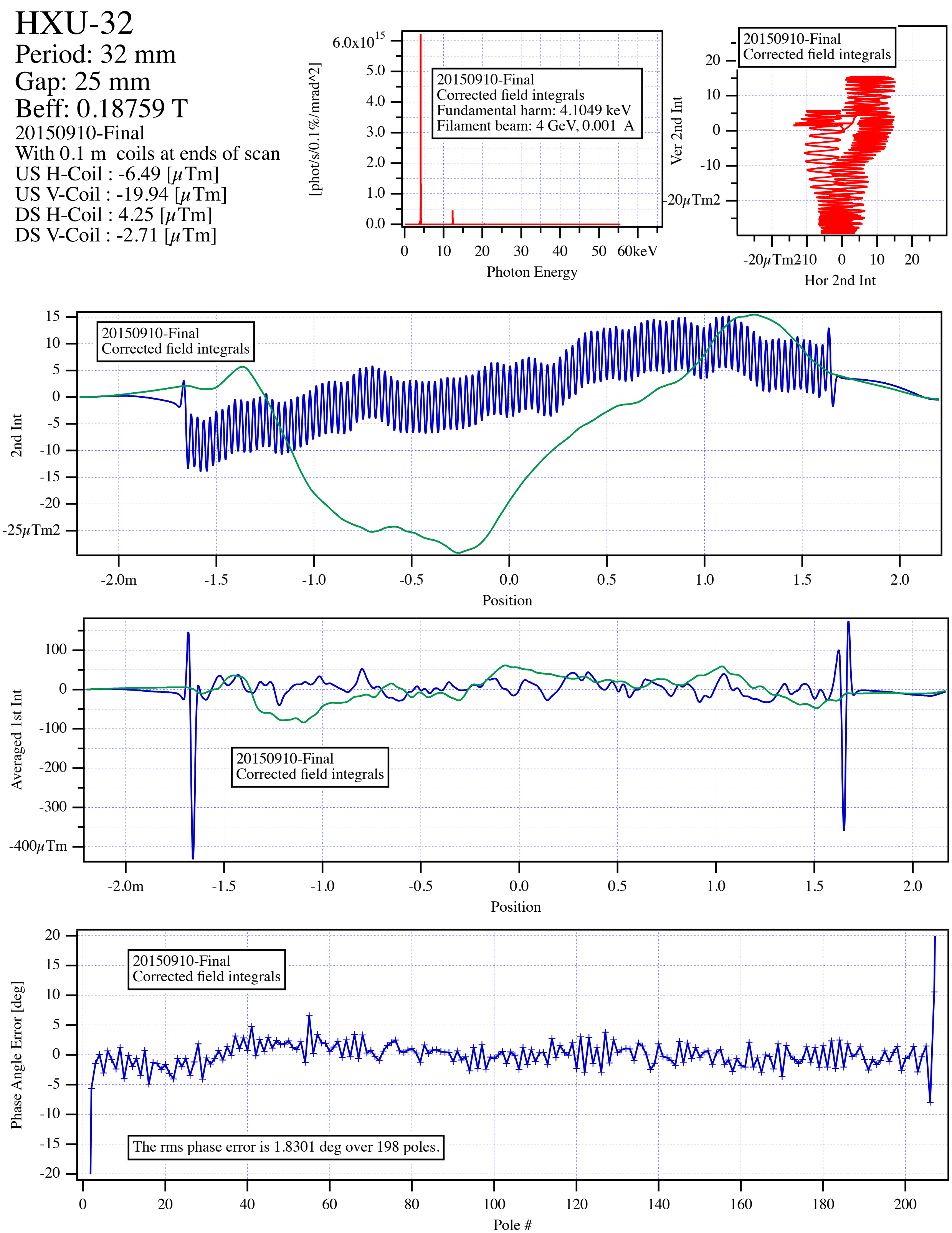

Figure 17: The measured fields, angles, trajectories and phase errors for the HXU-32 at 25 mm gap with the beam path corrected by virtual coils.

4.7 Gap 50, 100 and 180 mm

The measured vertical fields for the gaps 50, 100 and 180 mm are shown in Figure 18 and the corresponding horizontal fields are shown in Figure 19 .

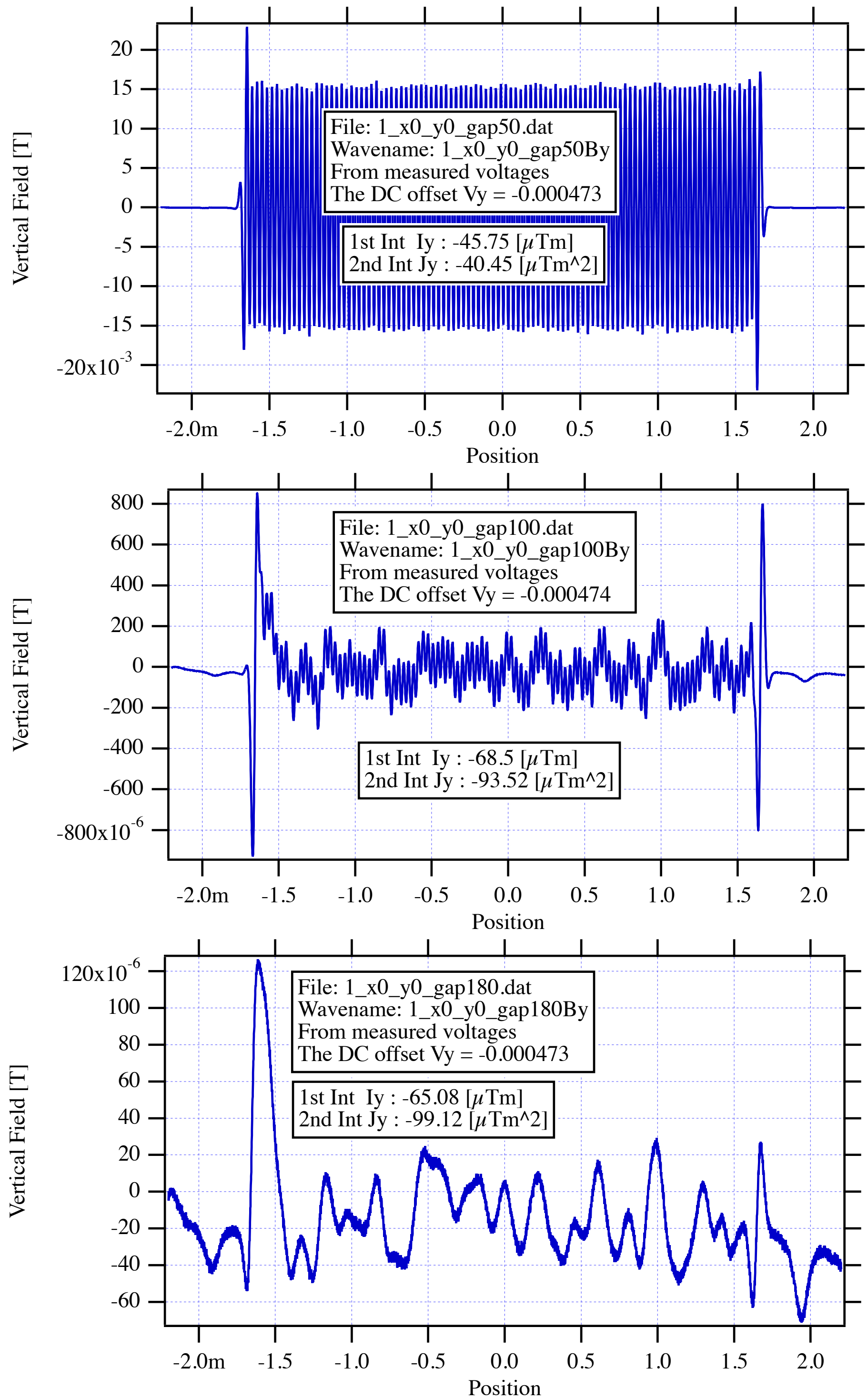

Figure 18: The measured vertical fields for the HXU-32 at the gaps 50, 100 and 180 mm.

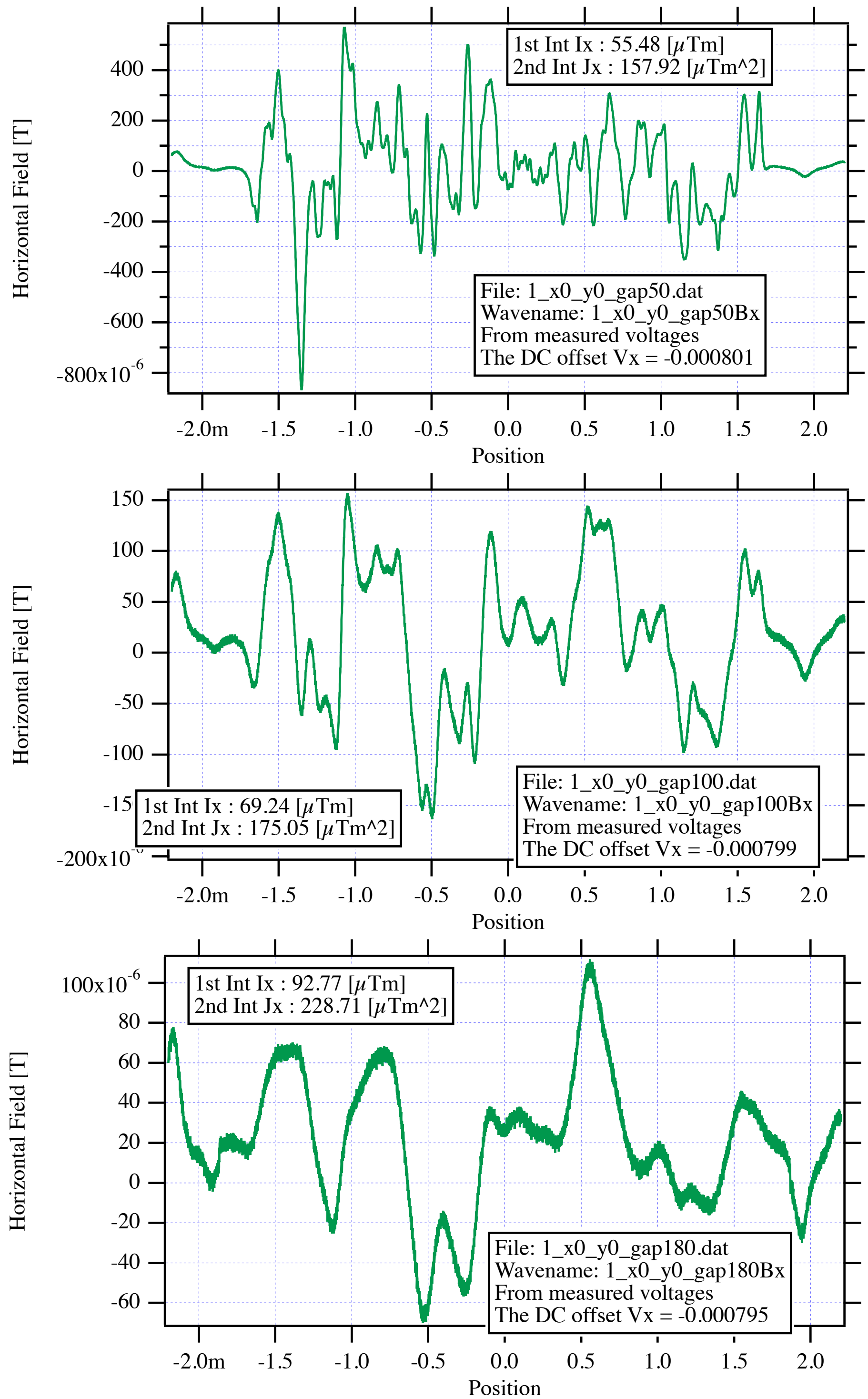

Figure 19: The measured horizontal fields for the HXU-32 at the gaps 50, 100 and 180 mm.

5 Repeatability of the effective field

The repeatability of the effective field has been measured by making 10 cycles over 8 gaps, giving in 80 measurements. The 8 gaps in the cycle ar 7.2, 8, 10, 15, 20, 15, 10, and 8 mm. The effective field has here, in the case of the repeatibilty measurements, been calculated using a fourier analysis of the measured magnetic fields.

Figure 20 shows the gaps during the repeatbility measurements. Figure 21 shows the measured effective field during the repeatbility measurements. Figure 22 shows the measured deviation of the effective field during the repeatbility measurements. Figure 23 shows the measured deviation of the effective field during the repeatbility measurements as a function of the gap.

Table 3 shows data from the repeatability measurements.

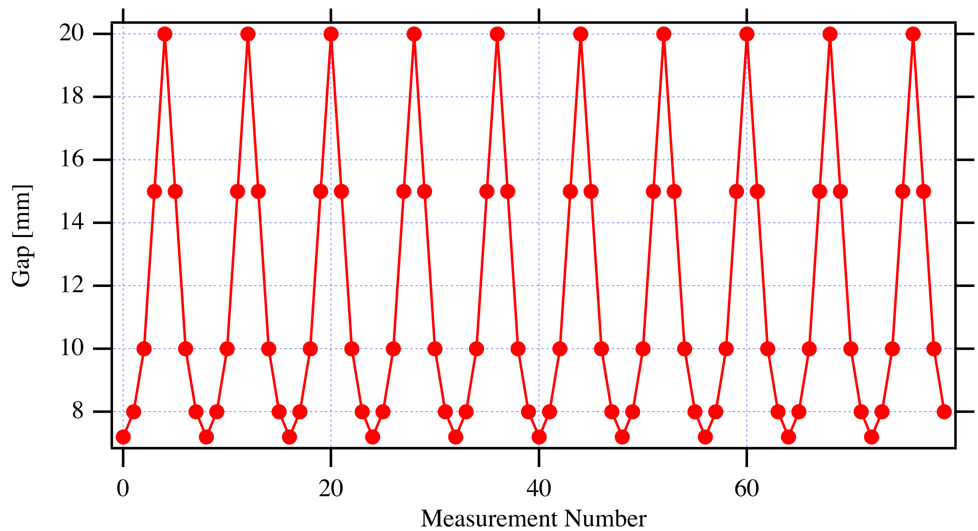

Figure 20: The gaps at the reapatability measurements of the effective field.

Table 3: Data from Beff repeatability measurements

Gap mm	Aver Beff T	RMS Dev G	RMS Dev $\times 10^{-4}$	Max ΔBeff/Beff $\times 10^{-4}$	Min ΔBeff/Beff $\times 10^{-4}$
7.2	1.2831	1.341	1.0451	1.5907	-1.3665
8	1.1594	0.93344	0.80513	0.80756	-2.0900
10	0.90420	0.48475	0.53611	0.93474	-1.0758
15	0.51764	0.23320	0.4505	0.93879	-0.65023
20	0.30890	0.13241	0.42864	0.50217	-0.64400

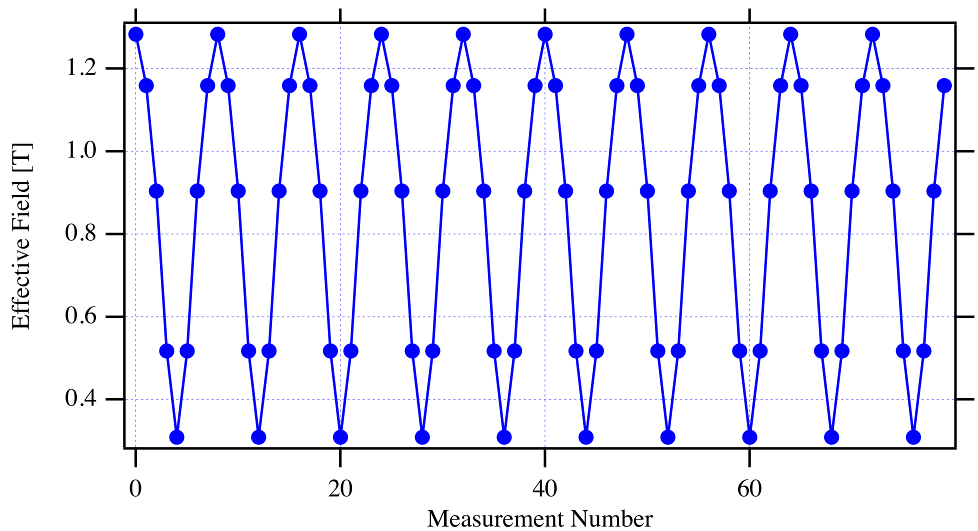

Figure 21: The measured effective field at the reapatability measurements.

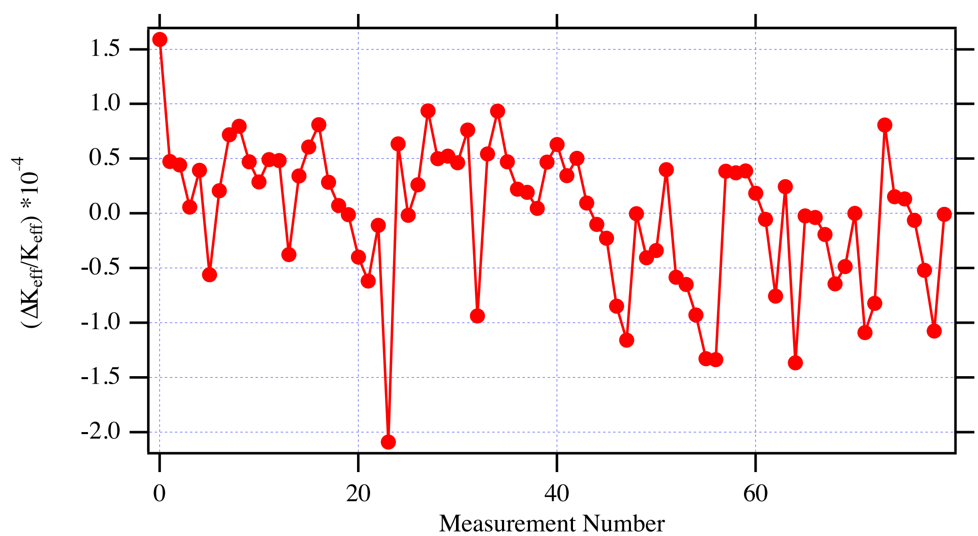

Figure 22: The measured deviation of the effective field at the reapatability measurements.

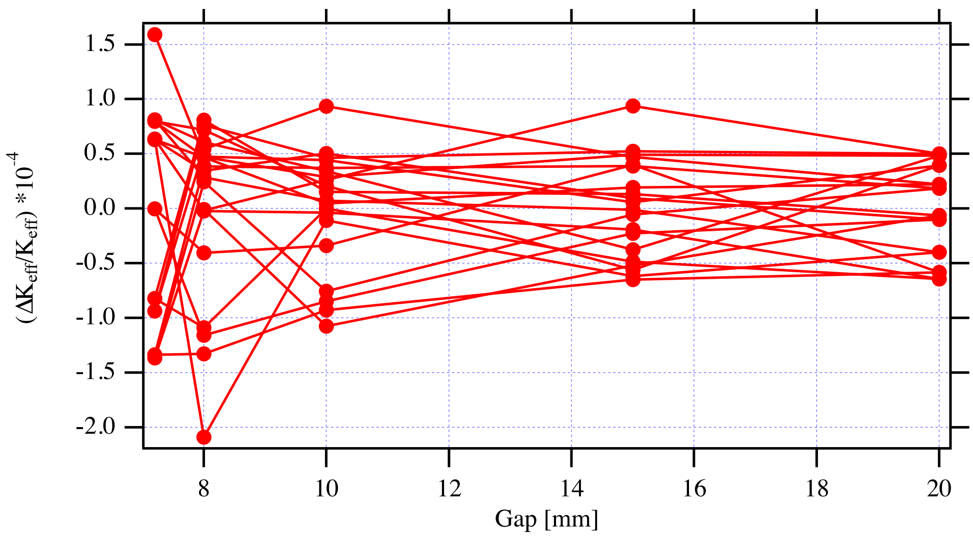

Figure 23: The measured deviation of the effective field at the reapatability measurements as a function of the gap.